

must be linked significantly (correlation P -value < 0.1 after correction for serial autocorrelation) to the US ACE index over each sub-period 1950–76 and 1977–2003, and for each year 1950 to 2003 after data excluding a 5-yr block centred on the year in question are excluded. This rule simulates the predictor selection process in an actual forecast situation.

Linear regression modelling

The US ACE index has a positively skewed (generalized Pareto) distribution. To satisfy the assumptions for using ordinary least squares regression, we transform this distribution to a normal distribution using the $\log(1 + \text{US ACE index})$ transform. We test for normality using the Kolmogorov–Smirnov test. The linear regression modelling is performed on these transformed data to produce hindcasts, which are then transformed back before the hindcast skill is computed. This procedure ensures that the observations are drawn from a normal distribution, and that the hindcast errors are normally distributed with a mean of zero (both requirements of linear regression modelling^{22,23}). A one-way analysis of variance (F -test) shows that the variance of the transformed observations and the variance of the hindcast errors are both constant in time (a further assumption of linear regression modelling^{22,23}).

The regression modelling is performed with a single predictor variable (the July wind index) rather than as a multiple regression with two or more predictor variables. Multiple regression is found always to give lower hindcast skill, the skill reduction increasing as the number of parameters increases. The single predictor (wind index) approach offers greater skill through better strengthening of the predictive signals and better removal of noise.

Cross-validated hindcasts

Cross-validated hindcasts are made with block elimination^{20,21}. The US ACE index of each year is hindcast by training the linear regression model on all data excluding a 5 yr block centred on the year of interest. The block is tapered at the time series ends. Block elimination is used to minimize potential skill inflation that might arise from multi-annual persistence. Cross-validation provides the best available estimate of forecast skill for the 54-yr sample.

Spearman rank correlation

The Spearman rank correlation coefficient is used as a robust and resistant alternative to the Pearson product–moment correlation coefficient²². The rank correlation is robust to deviations from linearity in a relationship, and is resistant to the influence of outliers.

Received 7 April 2004; accepted 31 January 2005; doi:10.1038/nature03454.

1. Benfield Industry Analysis and Research Team, *Catastrophe Losses* (Benfield, London, 2004).
2. Diaz, H. F. & Pulwarty, R. S. *Hurricanes: Climate and Socioeconomic Impacts* (Springer, Berlin, 1997).
3. Pielke, R. A. Jr & Landsea, C. W. Normalised hurricane damage in the United States: 1925–1995. *Weath. Forecast.* **13**, 621–631 (1998).
4. Lehmiller, G. S., Kimberlain, T. B. & Elsner, J. B. Seasonal prediction models for North Atlantic basin hurricane location. *Mon. Weath. Rev.* **125**, 1780–1791 (1997).
5. Gray, W. M., Landsea, C. W., Mielke, P. W. Jr & Berry, K. J. Predicting Atlantic basin seasonal tropical cyclone activity by 1 August. *Weath. Forecast.* **8**, 73–86 (1993).
6. Gray, W. M. Atlantic seasonal hurricane frequency. Part II: Forecasting its variability. *Mon. Weath. Rev.* **112**, 1669–1683 (1984).
7. Klotzbach, P. J. & Gray, W. M. Forecasting September Atlantic basin tropical cyclone activity. *Weath. Forecast.* **18**, 1109–1128 (2003).
8. Bove, M. C., Elsner, J. B., Landsea, C. W., Niu, X. & O'Brien, J. J. Effect of El Niño on U.S. landfalling hurricanes revisited. *Bull. Am. Meteorol. Soc.* **79**, 2477–2482 (1998).
9. Pielke, R. A. Jr & Pielke, R. A. Sr. La Niña, El Niño and Atlantic hurricane damages in the United States. *Bull. Am. Meteorol. Soc.* **80**, 2027–2034 (1999).
10. Saunders, M. A., Chandler, R. E., Merchant, C. J. & Roberts, F. P. Atlantic and NW Pacific typhoons: ENSO spatial impacts on occurrence and landfall. *Geophys. Res. Lett.* **27**, 1147–1150 (2000).
11. Lyons, S. W. U. S. tropical cyclone landfall variability 1950–2002. *Weath. Forecast.* **19**, 473–480 (2004).
12. Waple, A. M. et al. Climate assessment for 2001. *Bull. Am. Meteorol. Soc.* **83**, S1–S62 (2001).
13. Neumann, C. J., Jarvinen, B. R., McArdie, C. J. & Hammer, G. R. *Tropical Cyclones of the North Atlantic Ocean 1871–1998* (Historical Climatology Series 6–2, National Oceanic and Atmospheric Administration, Asheville, 1999).
14. Kalnay, E. et al. The NCEP/NCAR 40-year reanalysis. *Bull. Am. Meteorol. Soc.* **77**, 437–471 (1996).
15. Dong, K. & Neumann, C. J. The relationship between tropical cyclone motion and environmental geostrophic flows. *Mon. Weath. Rev.* **114**, 115–122 (1986).
16. Franklin, J. L., Feuer, S. E., Kaplan, J. & Aberson, S. Tropical cyclone motion and surrounding flow relationships: searching for beta gyres in Omega dropwindsonde datasets. *Mon. Weath. Rev.* **124**, 64–84 (1996).
17. Collins, D. J. & Lowe, S. P. A macro validation dataset for U.S. hurricane models. 217–252 (Casualty Actuarial Society, Winter Forum, 2001); available from CAS at (<http://www.casact.org/pubs>).
18. Davis, R. E. Predictability of sea surface temperatures and sea level pressure anomalies over the North Pacific Ocean. *J. Phys. Oceanogr.* **6**, 249–266 (1976).
19. Chen, W. Y. Fluctuations in northern hemisphere 700 mb height field associated with the Southern Oscillation. *Mon. Weath. Rev.* **110**, 808–823 (1982).
20. Elsner, J. B. & Schmertmann, C. P. Assessing forecast skill through cross-validation. *Weath. Forecast.* **9**, 619–624 (1994).
21. Standardised verification system (SVS) for long-range forecasts (LRF). *New Attachment II-9 to the Manual on the GDPS (WMO-No. 485)*, Vol. 1 (WMO, Geneva, 2002).
22. Wilks, D. S. *Statistical Methods in the Atmospheric Sciences* (Academic, San Diego, 1995).
23. Freund, R. J. & Wilson, W. J. *Regression Analysis: Statistical Modeling of a Response Variable* (Academic, San Diego, 1998).
24. Hilti, N., Saunders, M. A. & Lloyd-Hughes, B. Forecasting stronger profits. *Glob. Reinsurance* 6–7 (July/August 2004).

Acknowledgements We thank B. Lloyd-Hughes for help with Table 3 and other aspects of the work. J. B. Elsner, C. W. Landsea, F. Vitart, J. Heming and I. M. Mason are thanked for comments on the manuscript. This work is supported by the TSR (Tropical Storm Risk) venture sponsored by Benfield (an independent reinsurance intermediary), Royal & SunAlliance (an insurance group), and Crawford & Company (a claims management solutions company). We acknowledge NOAA-CIRES, Climate Diagnostics Center, Boulder, Colorado, for the NCEP/NCAR Global Reanalysis Project data, and NOAA's Hurricane Research Division for the HURDAT North Atlantic hurricane database.

Competing interests statement The authors declare that they have no competing financial interests.

Correspondence and requests for materials should be addressed to M.A.S. (mas@mssl.ucl.ac.uk).

Active out-of-sequence thrust faulting in the central Nepalese Himalaya

Cameron Wobus¹, Arjun Heimsath², Kelin Whipple¹ & Kip Hodges¹

¹Department of Earth, Atmospheric and Planetary Sciences, Massachusetts Institute of Technology, Cambridge, Massachusetts 02139, USA

²Department of Earth Sciences, Dartmouth College, Hanover, New Hampshire 03755, USA

Recent convergence between India and Eurasia is commonly assumed to be accommodated mainly along a single fault—the Main Himalayan Thrust (MHT)—which reaches the surface in the Siwalik Hills of southern Nepal^{1–3}. Although this model is consistent with geodetic^{4,5}, geomorphic⁶ and microseismic data⁷, an alternative model incorporating slip on more northerly surface faults has been proposed to be consistent with these data as well^{8–10}. Here we present *in situ* cosmogenic ¹⁰Be data indicating a fourfold increase in millennial timescale erosion rates occurring over a distance of less than 2 km in central Nepal, delineating for the first time an active thrust fault nearly 100 km north of the surface expression of the MHT. These data challenge the view that rock uplift gradients in central Nepal reflect only passive transport over a ramp in the MHT. Instead, when combined with previously reported ⁴⁰Ar–³⁹Ar data⁹, our results indicate persistent exhumation above deep-seated, surface-breaking structures at the foot of the high Himalaya. These results suggest that strong dynamic interactions between climate, erosion and tectonics have maintained a locus of active deformation well to the north of the Himalayan deformation front.

The central Nepalese Himalaya is a textbook example of continent–continent collision, in which the underthrusting of India has been concentrated on several roughly east–west-trending fault zones within a belt about 100 km wide. The northernmost of these fault zones is the Main Central Thrust (MCT), which marks a transition from the high-grade metamorphic Greater Himalayan Sequence in the north to the lower-grade Lesser Himalayan Sequence in the south. Geochronologic data indicate that the MCT is also the oldest structure, with evidence for initial activity on this thrust fault by 23–20 Myr ago¹¹. More southerly structures—the Main Boundary Thrust (MBT) and the Main Frontal Thrust (MFT)—developed progressively in a north–south sequence, consistent with observations in foreland fold and thrust belts worldwide¹² (Fig. 1a). Most researchers working in the Nepal orogen assume that recent surface faulting has been concentrated at the trace of the MFT, which defines the southern limit of deformation in the Himalayan system. In this model, the MFT absorbs almost all slip on the MHT. However, this interpretation does not provide a

direct explanation for the striking contrast between high modern surface uplift rates in the high Himalayan ranges and the much lower rates in the Himalayan foothills⁴, which occurs nearly 100 km north of the MFT across a distinctive physiographic transition. It has been suggested that these changes in physiography and surface uplift rate are best explained by a gradual ramp in the MHT in the middle crust^{1,4-6} (Fig. 1b).

While the ramp hypothesis is consistent with most geological and geophysical data from the Nepalese Himalaya, both the sharpness of the physiographic transition in central Nepal and the relatively abrupt change in surface uplift rate across it are difficult to reconcile with the broader transitions that might be expected as manifestations of a midcrustal ramp¹. In the Burhi Gandaki valley, for example, mean elevation and relief (as measured along a 20-km-wide swath profile) each increase more than twofold over a distance of less than 8 km (Fig. 2). The lower boundary of this physiographic transition can be precisely delineated on the basis of changes in valley morphology, hillslope gradients, channel gradients and the extent of thick alluvial fill deposits⁹. Importantly, this lower boundary occurs between 20 and 30 km south of the surface trace of the MCT, indicating that an unmapped thrust fault might be accommodating gradients in rock uplift in this valley. Farther west in the Marsyandi valley, changes in landscape morphology occur more gradually, which is consistent with a more broadly distributed strain field. In the Marsyandi drainage, the upper boundary of the physiographic transition is nearly coincident with the mapped trace of the MCT, indicating that strands of the MCT itself might be important in accommodating modern rock uplift gradients in

this valley¹⁰. These along-strike differences indicate spatial variations in how recent deformation is accommodated along the Himalayan front. Nonetheless, the physiographic data from central Nepal are all broadly consistent with independent evidence for recent deformation in the region including young, brittle shear zones near the MCT in the Marsyandi valley¹⁰ and sharp discontinuities in the patterns of Late Miocene–Quaternary ⁴⁰Ar–³⁹Ar and fission-track mineral cooling ages throughout central Nepal^{9,13,14}.

Unfortunately, although the physiographic transition is sharp and well defined in the Burhi Gandaki river, the poor quality of bedrock exposure makes it difficult to construct detailed structural maps to determine unequivocally whether young, surface-breaking faults are present. Here we report the results of a different approach to the problem based on deducing differences in erosional patterns from cosmogenic radionuclide data in detrital sediments. We measured concentrations of ¹⁰Be produced *in situ* in modern sediment from eight small tributaries to the Burhi Gandaki as a proxy for millennial timescale erosion rates in each catchment. The concentration of ¹⁰Be in quartz, interpreted with nuclide production rates scaled for altitude, latitude and local topography, enables erosion rates to be quantified at the outcrop scale¹⁵. At the basin scale, ¹⁰Be concentrations in sediment have been shown to represent reliable basin-average erosion rates in a variety of climatic and tectonic settings¹⁵⁻¹⁹. We use the spatial pattern of erosion rates from the Burhi Gandaki tributaries to delineate discontinuities in rock uplift rates across the range front. Field observations indicate that hillslope angles might approach threshold values near the physiographic transition, so landscape response should be rapid: as bedrock rivers adjust their incision rates in response to spatial variations in rock uplift, we expect the hillslopes to match this incision rate by landsliding to maintain their critical condition^{20,21}.

The calculation of a basin-average erosion rate from ¹⁰Be concentrations in sediment from steep, landslide-dominated catchments requires an assumption that the sediment collected at the basin outlet is well mixed, and therefore that pulses of cosmogenically ‘underexposed’ landslide-derived material are integrated into the bulk sediment sample. Larger basins will more effectively integrate these stochastic sediment pulses downstream, indicating that basin scale might be an important factor in controlling the fidelity of the cosmogenic signal²²⁻²⁴. Basins sampled for this study have drainage areas ranging from about 3 km² to about 22 km² (Table 1), a range in which preliminary numerical modelling suggests a high probability that basin-average erosion rates will be closely predicted—or only slightly underestimated—from detrital cosmogenic radionuclide concentrations²⁴. Furthermore, the drainage pattern in the Burhi Gandaki is trellised, with tributaries draining narrow (about 2–5 km wide) catchments subparallel to the structural grain of the orogen (Fig. 2a). Sediment from each tributary therefore records an estimate of the basin-average erosion rate from a narrowly constrained tectonostratigraphic position.

The ¹⁰Be data reveal a sharp discontinuity in erosion rates centred about 23 km south of the MCT, within the zone of the physiographic transition as defined by independent methods⁹. To the south of this discontinuity, erosion rates are uniform at about 0.2 mm yr⁻¹. To the north, erosion rates abruptly jump to about 0.8 mm yr⁻¹ and then gradually decline to about 0.2 mm yr⁻¹ over a distance of 10 km (Fig. 3a). ¹⁰Be concentrations (Table 1) indicate minimum exposure ages ranging from about 1 kyr to 3 kyr, indicating sharp spatial gradients in basin-average erosion rates over late Holocene timescales. This break in erosion rates is not correlated with any mappable break in lithology: rocks to the north and south of this transition each comprise phyllites and schists of the Lesser Himalayan sequence. Furthermore, there is no correlation between the cosmogenically determined erosion rates and basin size, and the fourfold increase in erosion rates is larger than any bias that might be predicted by preliminary modelling accounting for under-sampling of landslide-derived material in small catchments²⁴. The

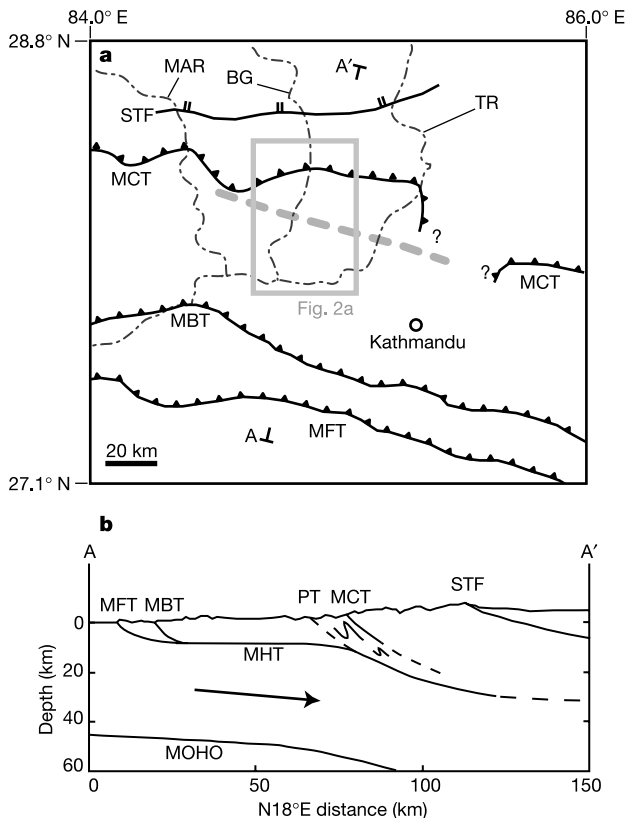


Figure 1 Geological setting. **a**, Regional geological map showing major tectonic structures and river systems. Dash-dotted lines: MAR, Marsyandi river; BG, Burhi Gandaki river; TR, Trisuli river. STF, South Tibetan fault. Dashed grey line shows the lower boundary of the physiographic transition where it is well defined (see the text for explanation). The grey box indicates the location of Fig. 2a. A–A' indicates the location of schematic cross section in **b**. **b**, Schematic cross section across central Nepal, showing the ramp in the MHT and the inferred projection of a fault at the physiographic transition (PT).

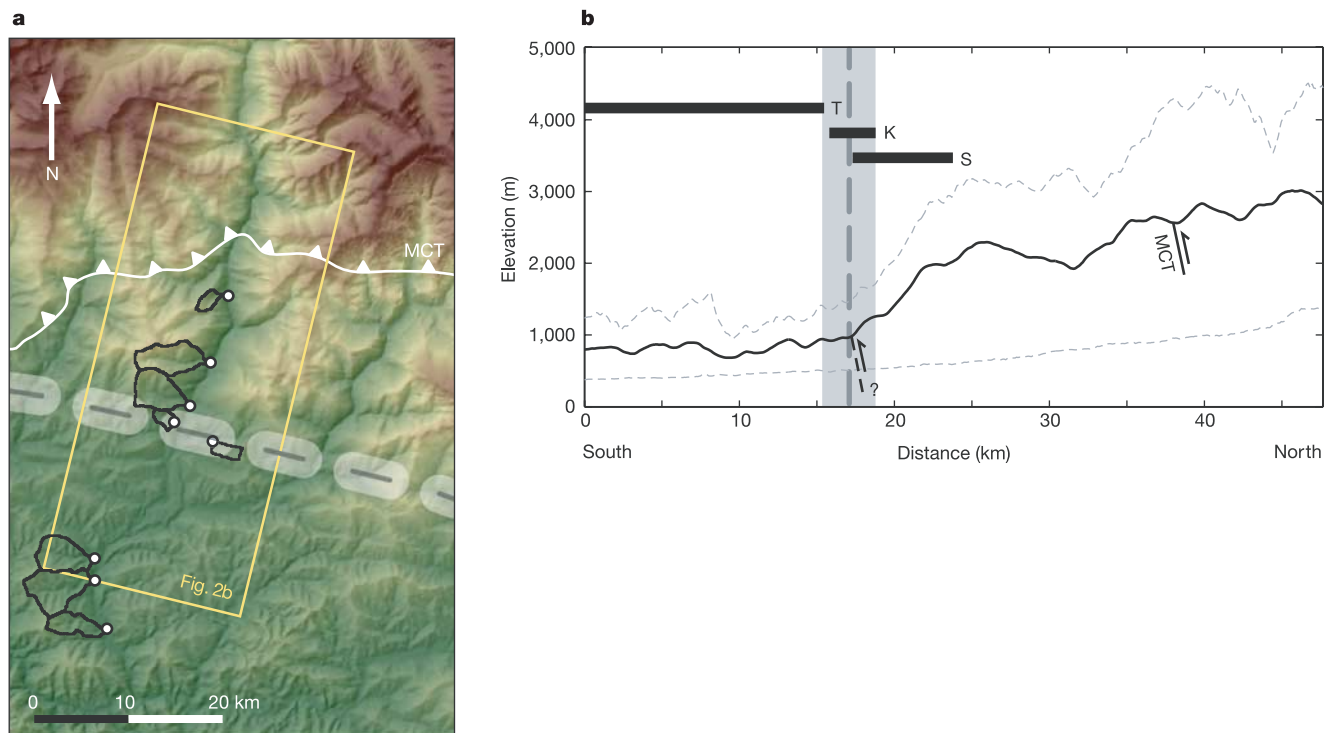


Figure 2 Sampling locations and study area physiography. **a**, Sample collection points (white dots) and drainage basins (black outlines). The dashed grey line shows approximate trace of the physiographic transition. The yellow rectangle delineates the boundaries of the swath profile shown in **b**. **b**, Mean (black line), minimum and maximum elevations

(dashed grey lines) along a 20-km-wide swath profile oriented orthogonal to the strike of the range. The vertical grey line marks the base of the physiographic transition (see text). Black bars show the extent of alluvial fill terraces (T), knickpoints on Burhi Gandaki tributaries (K) and the zone of increasing steepness on the Burhi Gandaki trunk stream (S).

spatial trend in ^{10}Be erosion rates therefore corroborates our interpretations of tectonics based solely on landscape morphology, and allows us to constrain more narrowly the locus of active thrust faulting in the Burhi Gandaki valley.

The discontinuity in short-term erosion rates is also co-located with a prominent break in long-term cooling rates from thermochronology (Fig. 3b): to the north of the physiographic transition, muscovite ^{40}Ar – ^{39}Ar cooling ages are young (Cenozoic), whereas they are substantially older to the south (Palaeozoic–Proterozoic)⁹. Calculation of long-term exhumation rates from these data would require a detailed thermal model accounting for lateral advection of rock and temporal variations in the subsurface thermal structure. Although this calculation is beyond the scope of this study, the abrupt discontinuity in cooling ages is a robust finding that corroborates our interpretation of a surface-breaking thrust fault at the physiographic transition. Furthermore, the thermochronologic data provide the additional constraint that active thrust faulting has persisted at least long enough to create a substantial discontinuity in the total depth of exhumation from north to south.

The presence of a tectonically significant, thrust-sense fault zone at the physiographic transition, as implied by the spatial

coincidence of breaks in short-term (cosmogenic) and long-term (^{40}Ar – ^{39}Ar) erosion rates, is consistent with field observations of brittle deformational fabrics parallel to the northward-dipping foliations in the Lesser Himalayan Sequence⁹. Physiographic data from along strike suggest that this fault zone extends eastwards to the Trisuli valley, maintaining its position substantially south of the MCT. To the west of the Burhi Gandaki valley, the orientation of the physiographic transition and the more diffuse gradients in landscape morphology suggest that this fault zone becomes more broadly distributed in the Marsyandi valley, and might correspond to recent activity within the MCT zone^{10,14}.

We speculate that the origin of this fault zone might be intimately tied to the presence of strong precipitation gradients across the central Nepalese Himalaya. Focused monsoonal precipitation is well documented on the southern flank of the Nepalese Himalaya^{14,25} and has been posited to drive localized tectonic uplift by removing mass from the top of an extruding ductile channel^{26,27}. Although the energy driver for this channel extrusion is gravitational potential energy from the Tibetan plateau, erosion must be important in determining where the energy is dissipated. Our data suggest there might be a dynamic feedback between climate and tectonics in the

Table 1 Basin characteristics and cosmogenic erosion rate data

| Sample | Distance from MCT (km)* | Drainage area (km ²) | Mean slope (deg)† | Elevation range (m)‡ | Mass of quartz (g) | [¹⁰ Be] (10 ³ atoms g ⁻¹) | Erosion rate (mm yr ⁻¹) |
|--------|-------------------------|----------------------------------|-------------------|----------------------|--------------------|--|-------------------------------------|
| 01WBS5 | 7.0–10.0 (7.5) | 3.4 | 28.4 | 797–2,372 | 58.64 | 42.1 ± 2.3 | 0.19 ± 0.02 |
| 01WBS6 | 13.5–17.5 (15.0) | 18.4 | 30.8 | 604–3,158 | 79.32 | 27.8 ± 1.6 | 0.37 ± 0.04 |
| 01WBS7 | 17.0–21.5 (19.5) | 17.5 | 24.6 | 533–2,455 | 69.25 | 13.9 ± 1.7 | 0.48 ± 0.08 |
| 03WBS1 | 21.0–23.0 (22.0) | 3.2 | 21.4 | 643–1,325 | 150.90 | 6.0 ± 0.5 | 0.77 ± 0.10 |
| 03WBS2 | 22.0–24.0 (23.0) | 3.9 | 17.6 | 723–1,475 | 150.24 | 27.9 ± 0.9 | 0.19 ± 0.01 |
| 01WBS3 | 37.0–41.5 (38.5) | 16.7 | 22.0 | 413–1,412 | 67.14 | 21.9 ± 1.9 | 0.19 ± 0.03 |
| 01WBS2 | 40.0–46.0 (41.0) | 22.4 | 21.9 | 370–1,574 | 70.03 | 23.4 ± 1.8 | 0.19 ± 0.02 |
| 01WBS1 | 44.5–47.0 (45.5) | 10.5 | 21.4 | 348–1,670 | 84.88 | 25.4 ± 1.7 | 0.18 ± 0.02 |

Errors are ± 1σ.

*Distance to the northern and southern edges of the basin, rounded to the nearest 0.5 km and projected onto a line oriented N18°E. Numbers in parenthesis are distances to the basin outlet.

† Slopes calculated from a 3 × 3 moving window over 90-m resolution digital elevation model (DEM).

‡ Production rates calculated pixel by pixel by using 90-m DEM.

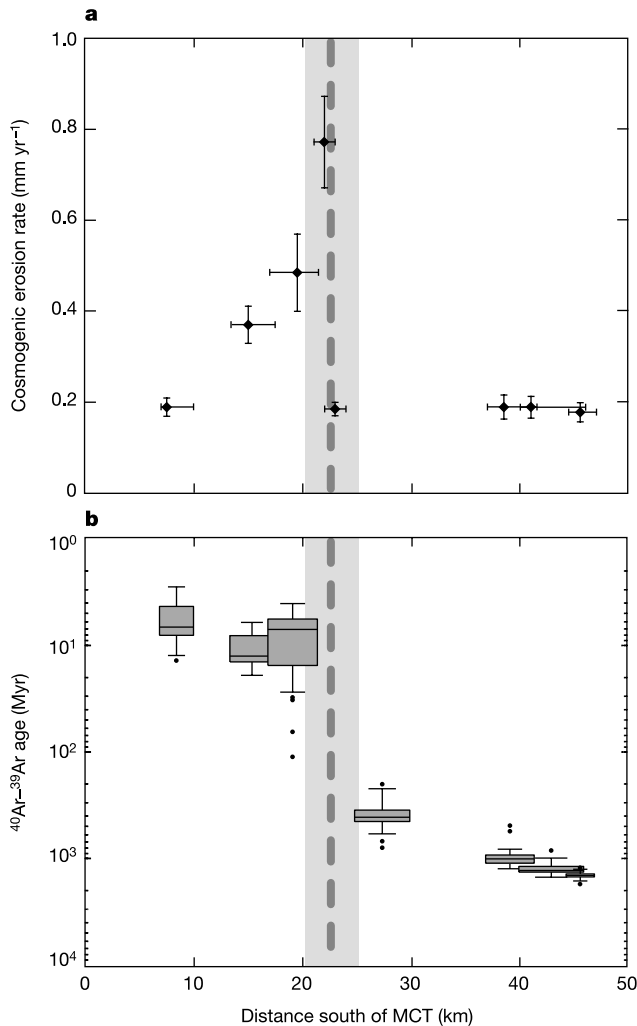


Figure 3 Erosion rate and cooling-age data. **a**, Plot of ¹⁰Be erosion rate (dots) against distance from the MCT, projected onto a N18°E line. Error bars on the x axis represent the projected distance to basin limits; error bars on the y axis represent 1σ uncertainty in analytical results. **b**, Plot of ⁴⁰Ar-³⁹Ar cooling ages (logarithmic scale) against distance from the MCT. Shaded boxes, vertical whiskers, and horizontal lines within boxes represent the interquartile range, limits of analysis results, and median values, respectively. Black dots represent outliers (more than 1.5 times the interquartile range beyond box limits). Widths of boxes represent widths of individual basins. Complete data can be found in ref. 9. Vertical shading and dashed lines show physiographic transition.

Himalayan orogen, so much so that the locus of deep exhumation has been maintained nearly 100 km northwards of the Himalayan thrust front. This focused exhumation sustains the marked topographic front of the high Himalaya, and increases the efficiency of energy dissipation from the Himalayan system. □

Received 14 October 2004; accepted 23 February 2005; doi:10.1038/nature03499.

- Cattin, R. & Avouac, J. P. Modeling mountain building and the seismic cycle in the Himalaya of Nepal. *J. Geophys. Res.* **105**, 13389–13407 (2000).
- Lave, J. & Avouac, J. P. Active folding of fluvial terraces across the Siwaliks Hills, Himalayas of central Nepal. *J. Geophys. Res.* **105**, 5735–5770 (2000).
- Pandey, M. R., Tandukar, R. P., Avouac, J. P., Lave, J. & Massot, J. P. Interseismic strain accumulation on the Himalayan crustal ramp (Nepal). *Geophys. Res. Lett.* **22**, 751–754 (1995).
- Jackson, M. & Bilham, R. Constraints on Himalayan deformation inferred from vertical velocity fields in Nepal and Tibet. *J. Geophys. Res.* **99**, 13897–13912 (1994).
- Bilham, R. *et al.* GPS measurements of present-day convergence across the Nepal Himalaya. *Nature* **386**, 61–64 (1997).
- Lave, J. & Avouac, J. P. Fluvial incision and tectonic uplift across the Himalayas of central Nepal. *J. Geophys. Res.* **106**, 26561–26591 (2001).
- Pandey, M. R. *et al.* Seismotectonics of the Nepal Himalaya from a local seismic network. *J. Asian Earth Sci.* **17**, 703–712 (1999).

- Catlos, E. J. *et al.* Geochronologic and thermobarometric constraints on the evolution of the Main Central Thrust, central Nepal Himalaya. *J. Geophys. Res.* **106**, 16177–16204 (2001).
- Wobus, C. W., Hodges, K. V. & Whipple, K. X. Has focused denudation sustained active thrusting at the Himalayan topographic front? *Geology* **31**, 861–864 (2003).
- Hodges, K., Wobus, C., Ruhl, K., Schildgen, T. & Whipple, K. Quaternary deformation, river steepening and heavy precipitation at the front of the Higher Himalayan ranges. *Earth Planet. Sci. Lett.* **220**, 379–389 (2004).
- Hodges, K. V. Tectonics of the Himalaya and southern Tibet from two perspectives. *GSA Bull.* **112**, 324–350 (2000).
- DeCelles, P. G. *et al.* Stratigraphy, structure, and tectonic evolution of the Himalayan fold-thrust belt in western Nepal. *Tectonics* **20**, 487–509 (2001).
- Copeland, P. *et al.* An early Pliocene thermal disturbance of the Main Central Thrust, central Nepal; implications for Himalayan tectonics. *J. Geophys. Res.* **96**, 8475–8500 (1991).
- Burbank, D. W. *et al.* Decoupling of erosion and climate in the Himalaya. *Nature* **426**, 652–655 (2003).
- Bierman, P. R. & Nichols, K. K. Rock to sediment-slope to sea with ¹⁰Be-rates of landscape change. *Annu. Rev. Earth Planet. Sci.* **32**, 215–255 (2004).
- Brown, E. T., Stallard, R. F., Larsen, M. C., Raisbeck, G. M. & Yiou, F. Denudation rates determined from the accumulation of in-situ produced ¹⁰Be in the Luquillo Experimental Forest, Puerto Rico. *Earth Planet. Sci. Lett.* **129**, 193–202 (1995).
- Riebe, C. S., Kirchner, J. W., Granger, D. E. & Finkel, R. C. Erosional equilibrium and disequilibrium in the Sierra Nevada, inferred from cosmogenic ²⁶Al and ¹⁰Be in alluvial sediment. *Geology* **28**, 803–806 (2000).
- Schaller, M., von Blanckenburg, F., Hovius, N. & Kubik, P. W. Large-scale erosion rates from in-situ produced cosmogenic nuclides in European river sediments. *Earth Planet. Sci. Lett.* **188**, 441–458 (2001).
- Vance, D., Bickle, M., Ivy-Ochs, S. & Kubik, P. W. Erosion and exhumation in the Himalaya from cosmogenic isotope inventories in river sediments. *Earth Planet. Sci. Lett.* **206**, 273–288 (2003).
- Burbank, D. W. *et al.* Bedrock incision, rock uplift and threshold hillslopes in the northwestern Himalayas. *Nature* **379**, 505–510 (1996).
- Roering, J. J., Kirchner, J. W. & Dietrich, W. E. Hillslope evolution by nonlinear, slope-dependent transport: steady state morphology and equilibrium adjustment timescales. *J. Geophys. Res.* **106**, 16499–16513 (2001).
- Bierman, P. & Steig, E. Estimating rates of denudation using cosmogenic isotope abundances in sediment. *Earth Surf. Processes Landforms* **21**, 125–139 (1996).
- Granger, D. E., Kirchner, J. W. & Finkel, R. Spatially averaged long-term erosion rates measured from in situ-produced cosmogenic nuclides in alluvial sediment. *J. Geol.* **104**, 249–257 (1996).
- Niemi, N. A., Oskin, M. E. & Burbank, D. A numerical simulation of the effects of mass-wasting on cosmogenically determined erosion rates. *Eos* **85** (Fall Meet. Suppl.), Abstract H51C-1157 (2004).
- Putkonen, J. Continuous snow and rain data at 500 to 4400 m altitude near Annapurna, Nepal, 1999–2001. *Arct. Antarct. Alpine Res.* **36**, 244–248 (2004).
- Beaumont, C., Jamieson, R. A., Nguyen, M. H. & Lee, B. Himalayan tectonics explained by extrusion of a low-viscosity crustal channel coupled to focused surface denudation. *Nature* **414**, 738–742 (2001).
- Hodges, K. V., Hurtado, J. M. & Whipple, K. X. Southward extrusion of Tibetan crust and its effect on Himalayan tectonics. *Tectonics* **20**, 799–809 (2001).

Acknowledgements We thank D. Burbank and P. Bierman for constructive reviews, which greatly improved the quality of the original manuscript, R. Finkel at LLNL for accommodating our samples at short notice, and B. Crosby, K. Ruhl, T. Schildgen, N. Wobus and Himalayan Experience for field assistance. The work was funded by NSF and NSF Continental Dynamics.

Competing interests statement The authors declare that they have no competing financial interests.

Correspondence and requests for materials should be addressed to C.W. (cwobus@mit.edu).

Geobiology of a microbial endolithic community in the Yellowstone geothermal environment

Jeffrey J. Walker, John R. Spear & Norman R. Pace

Department of Molecular, Cellular and Developmental Biology and the Center for Astrobiology, University of Colorado, Boulder, Colorado 80309-0347, USA

The endolithic environment, the pore space of rocks, is a ubiquitous habitat for microorganisms on the Earth¹ and is an important target of the search for life elsewhere in the Solar System². Photosynthetic, endolithic microbial communities commonly inhabit the outer millimetres to centimetres of all rocks exposed to the Earth's surface. In the most extreme terrestrial climates, such as hot and cold deserts, endolithic microorganisms are often the main form of life^{3–5}. The endolithic microhabitat